IJMMM International Journal of Minerals, Metallurgy and Materials 矿物冶金与材料学报（英文版）

Corrosion, mechanical and microstructural properties of aluminum 7075–carbon nanotube nanocomposites for robots in corrosive environments

Arun David, Satheesh Kumar Gopal, Poovazhagan Lakshmanan, and Amith Sukumaran Chenbagam

Cite this article as:
Arun David, Satheesh Kumar Gopal, Poovazhagan Lakshmanan, and Amith Sukumaran Chenbagam, Corrosion, mechanical and microstructural properties of aluminum 7075–carbon nanotube nanocomposites for robots in corrosive environments, *Int. J. Miner. Metall. Mater.*, 30(2023), No. 6, pp. 1140-1151. https://doi.org/10.1007/s12613-022-2592-3

View the article online at SpringerLink or IJMMM Webpage.

International Journal of Minerals, Metallurgy and Materials
Volume 30, Number 6, June 2023, Page 1140
https://doi.org/10.1007/s12613-022-2592-3

Corrosion, mechanical and microstructural properties of aluminum 7075–carbon nanotube nanocomposites for robots in corrosive environments

Arun David, *Satheesh Kumar Gopal*✉, *Poovazhagan Lakshmanan*, *and Amith Sukumaran Chenbagam*

Sri Sivasubramaniya Nadar College of Engineering, Kalavakkam, Chennai–603110, India
(Received: 28 September 2022; revised: 10 December 2022; accepted: 25 December 2022)

Abstract: The introduction of in-pipe robots for sewage cleaning provides researchers with new options for pipe inspection, such as leakage, crack, gas, and corrosion detection, which are standard applications common in the current industrial scenario. The question that is frequently overlooked in all these cases is the inherent resistance of the robots to corrosion. The mechanical, microstructural, and corrosion properties of aluminum 7075 incorporated with various weight percentages (0, 0.5wt%, 1wt%, and 1.5wt%) of carbon nanotubes (CNTs) are discussed. It is fabricated using a rotational ultrasonication with mechanical stirring (RUMS)-based casting method for improved corrosion resistance without compromising the mechanical properties of the robot. 1wt% CNTs–aluminum nanocomposite shows good corrosion and mechanical properties, meeting the requirements imposed by the sewage environment of the robot.

Keywords: aluminum 7075; carbon nanotubes; rotational ultrasonication with mechanical stirring; mechanical characterization; microstructure; robot

1. Introduction

Scavenging is one domain field despite human assistance, existing machines are often insufficient to clear the sewers in important cities around the globe. The robots have grown in complexity since their initial objective of ensuring minimum contact with sewage waste while cleaning. The complexity grew over time owing to the presence of other assorted garbage, such as wrapping, polythene bags, and plastic bottles. Thus, the current generation of researchers is focused on the trade-off between the initial cost and its operational cost. A thorough investigation of the corrosion and mechanical properties of a robot is pursued in this study to ensure the longevity of the robot in a hazardous environment.

Researchers have recently focused on developing ultra-high-strength materials, particularly lightweight ones, that can match the stiffness, wear resistance, and corrosion resistance of general engineering materials [1–4]. Although aluminum and its alloys play an important role in industrial applications. Alumina oxide, silicon carbide, and boron carbide are some of the most prominent strengthening materials used in aluminum nanocomposites (ANCs) [5–10]. Despite the improved mechanical characteristics of ANCs, their broad usage beyond the saturation limit remains hindered by the effect of nanoparticles on corrosion resistance. Even the protective oxide layer gets destroyed when the appropriate proportion of nanoparticles is exceeded, leading to discontinuity and severe corrosion. The corrosion resistance of ANCs is influenced by various parameters, including porosity, types of nanoparticles, the number of particles used, the property of the material, microcracks, residual stress, brittle intermetallic phases, and processing methods [11–12]. Studies on corrosion were conducted using various reinenforcement particles, including silicon carbide [11–12], boron carbide [13], magnesium alloys (2%–8%) [14], and T6 heat-treated alloys [15].

The use of multiwall carbon nanotubes (MWCNTs) in composite materials is the most promising aspect of all the nanomaterials that have been studied. Various studies have reported that CNTs can achieve excellent mechanical properties at a high temperature without losing the mechanical strength and stiffness of a metal matrix, hence, CNTs are a feasible reinforcement [16–24].

From the few studies that employ CNTs as a reinforcement, it is understood that performance of CNTs are strongly influenced by the fabrication methods adopted. Stir casting [23], powder metallurgy [24], squeeze casting [25], spray casting [26], and other fabrication processes are commonly employed in the fabrication of ANCs. Stir casting is commonly used to manufacture ANCs because it is simple, cost-effective, and applicable to large-scale production, however, this method has the drawbacks of causing particle agglomeration and porosity present in the composites [27]. Amith *et al*. [28] investigated the aluminum 7075 (Al7075) alloy with hexagonal boron nitrate (h-BN) nanoparticles using a

✉ Corresponding author: Satheesh Kumar Gopal E-mail:satheeshkumarg@ssn.edu.in

rotational ultrasonication with mechanical stirring (RUMS) method, and it shows the ANCs fabricated through RUMS method has high strength, hardness, and fine-grain refinement compared to that of fabricating by the mechanical stirrer method and the conventional ultrasonication-assisted casting technique. The RUMS method was adopted to fabricate Al7075 nanocomposites reinforced with varying CNTs weight percentage (0, 0.5wt%, 1wt%, and 1.5wt%) in this study because it demonstrated promising characteristics in avoiding particle agglomeration. To further improve the corrosion characteristics, the effect of heat treatment is also included in this study. The samples are examined in an acetic acid solution (a major acid content in sewage water) to study the mechanical, corrosion, and microstructural properties of the Al–CNTs composite.

2. Experimental

2.1. Materials

The Al7075 alloy used in this study is obtained from Perfect Metals Works in Bangalore. The reinforcement material used is CNTs (Sisco Research Laboratories in Maharashtra, India). The chemical composition of Al7075 is determined using optical emission spectroscopy, as shown in Table 1.

CNTs (99.9% purity) have a fixed density of 2.2 g·cm^{-3} and diameter of 4–20 nm, as shown in Fig. S1 (see the Supplementary information). Fig. 1(a–b) shows the transmittee electron microscopy (TEM) images of multiwall CNTs, and Fig. 1(c–d) shows the X-ray diffraction (XRD) analysis and Raman spectrum of the CNTs, respectively, and the XRD and Raman spectra are explained in the supplementary information file.

2.2. Fabrication process

The Al7075 alloy reinforced with CNTs is synthesized using the RUMS process. The supplementary information shows the photo of an RUMS machine (Fig. S2) and a schematic of the RUMS casting process (Fig. S3).

After the RUMS process, the ANCs underwent a T6 heat treatment process. Table 2 shows the amount of reinforcement in the ANCs samples along with the notations. These samples were used for further mechanical, corrosion, and microstructural studies.

Table 1. Chemical composition of Al7075 wt%

Zn	Mg	Cu	Cr	Fe	Ti	Si	Sn	Mn	Al
5.280	2.325	1.703	0.202	0.089	0.035	0.036	0.019	0.011	Bal.

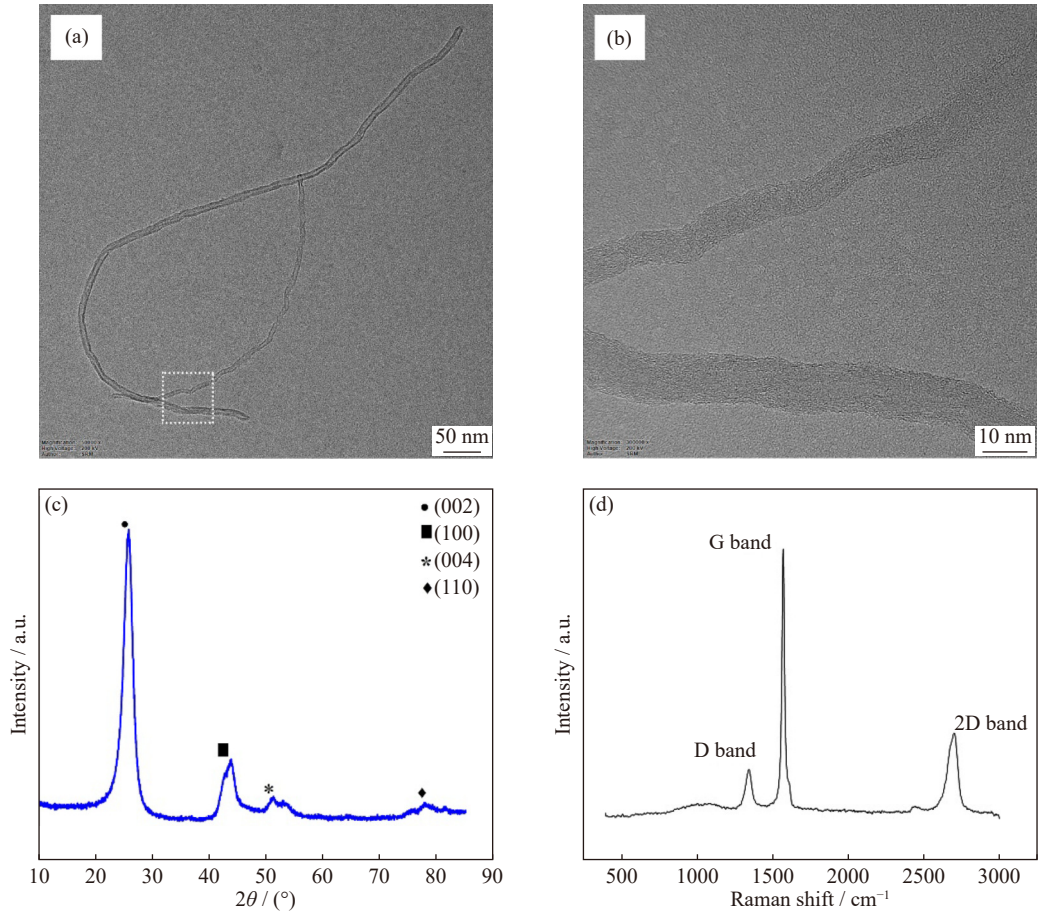

Fig. 1. (a–b) Transmission electron microscopy (TEM) images of CNTs, (c) XRD analysis of CNTs, and (d) Raman spectra of CNTs.

Table 2. Amount of reinforcement in the aluminum matrix and the notations

As-cast samples	Notation	T6 heat-treated samples	Notation
Al7075–0 CNTs	A_0	T6-Al7075–0 CNTs	T_0
Al7075–0.5wt% CNTs	$A_{0.5}$	T6-Al7075–0.5wt% CNTs	$T_{0.5}$
Al7075–1wt% CNTs	A_1	T6-Al7075–1wt% CNTs	T_1
Al7075–1.5wt% CNTs	$A_{1.5}$	T6-Al7075–1.5wt% CNTs	$T_{1.5}$

2.3. Mechanical testing

Nanocomposite ingots are cut to prepare the specimens for the Vickers microhardness test (ASTM E92), tensile test for sub-sized samples (ASTM E8), and Charpy impact test (ASTM E23) as per ASTM standards. Following the tests, the fractography analysis of the fractured sample surfaces was conducted using scanning electron microscopy (SEM) to identify the failure mechanism.

2.4. Corrosion test

The corrosion tests performed on the as-cast as well as solutionized and aged (T6) ANCs samples are static immersion corrosion test (ASTM G31), salt fog spray test (ASTM G85), and potentiodynamic polarization test (ASTM G59) standards. The weight loss is calculated and expressed as the rate of corrosion, given in millimeters per year ($mm \cdot a^{-1}$). The corroded surfaces are evaluated using SEM. The experiment duration and various percentage of acid solution are described in the supplementary information file.

2.5. Microstructural characterization

An optical microscope is used to examine the microstructures, grain refinement, and average grain size (AGS) measurements of the ANCs. SEM is used to examine the fractography of the tested-tensile sample and evaluate nanoparticle dispersion in the Al matrix. The particles present in the ANCs and the second-phase matrix are determined using SEM-energy dispersive spectroscopy (EDS). Transmission electron microscopy (TEM) reveals dislocation density, the presence of CNTs, precipitates, and CNTs/Al matrix interface bonding. The presence of particles in the ANCs fabricated using the RUMS method is confirmed using XRD. Keller's reagent (HF = 4 mL, HCl = 6 mL, HNO_3 = 8 mL, H_2O = 82 mL) is used to etch the specimens.

2.6. Density, porosity, and average grain size measurements

The densities of ANCs are calculated using the rule of mixtures and Archimedes' principle, as shown in Eqs. (1–2).

$$\frac{1}{\rho_{TD}} = \left\{\frac{W_{MM}}{\rho_{MM}} + \frac{W_{RM}}{\rho_{RM}}\right\} \tag{1}$$

$$\rho_{ED} = \left(\frac{W_{NA}}{W_{NA} - W_{NW}}\right) \tag{2}$$

where ρ_{TD} is the theoretical density of the nanocomposite, $g \cdot cm^{-3}$; ρ_{ED} is the experimental density of the nanocomposite, $g \cdot cm^{-3}$; W_{MM} is the weight fraction of the matrix material; W_{RM} is the weight fraction of the reinforcement material; ρ_{MM} is the density of the matrix material; ρ_{RM} is the density of the reinforcement material; W_{NA} is the mass of the nanocomposite in air, g; and W_{NW} is the mass of the nanocomposite in water, g.

$$\text{Porosity} = \left(\frac{\rho_{TD} - \rho_{ED}}{\rho_{TD}}\right) \times 100\% \tag{3}$$

Eq. (3) is used to calculate the proportions of porosity in nanocomposites. According to ASTM E112, the linear intercept method is used to determine the AGS. The open-source ImageJ tool is used to determine the length of the linear line.

3. Results and discussion

3.1. Density and porosity

Since CNTs have a lower density than the Al7075 alloy, the theoretical densities of ANCs decrease as the content of CNTs increases. The percentage porosity trend shows a decrease in the experimental densities (calculated by Archimedes' principle) for different compositions of the nanocomposites, as shown in Table 3. The degasifying action of rotating ultrasonication causes decrease in porosity percentage, as it allows the CNTs to scatter entirely in the Al matrix without forming voids. With the further addition of CNTs, the experimental density of nanocomposite decreased, indicating the presence of casting voids caused by the agglomeration of CNTs, as shown in Table 3 [29].

3.2. Microstructure characteristics

3.2.1. Optical microscopy

The major elements of the ANCs microstructure are α-Al and eutectic phases. Optical microscopy images show that the alloying components and precipitates are separated at the grain boundary, as shown in Fig. 2. The addition of CNTs to the ANCs causes grain size reduction.

Table 3. Density, porosity, and average grain size of ANCs

Nanocomposite	Experimental density / ($g \cdot cm^{-3}$)	Theoretical density / ($g \cdot cm^{-3}$)	Porosity / %	AGS / μm
A_0	2.7482	2.8100	1.90	43.4
$A_{0.5}$	2.7637	2.8058	1.30	35.9
A_1	2.7815	2.8019	0.56	32.4
$A_{1.5}$	2.7733	2.7988	0.85	39.8

3.2.2. SEM and EDS analysis

Fig. 3(a–d) shows the morphology and the dispersion of different content of CNTs in the ANCs, establishing a uniform dispersion of CNTs in the matrix without forming clusters. Liao *et al.* [30] performed mechanical investigations and observed severe agglomerations and wider voids in the nanocomposite reinforced with 1.5wt% of CNTs, resulting in a decrease in strength and microhardness values. Finer grains are observed in A_1 nanocomposite because of lower proportions of α-Al phases and comparatively widespread eutectic phases. During the solutionizing and aging processes of the ANCs, the eutectic phases are partly soluble, resulting in the formation of second-phase particles with excess eutectic phases. The EDS analysis of the $A_{1.5}$ nanocomposite shows the presence of key alloying elements Al, Zn, Mg, Cu, and C for the 1.5wt% CNTs content in the ANCs (Fig. 3(e)), confirming the elements present in the nanocomposites listed in Table 1. In addition, the carbon element is also observed in the Al matrix for A_1 ANCs, as shown in Fig. 4.

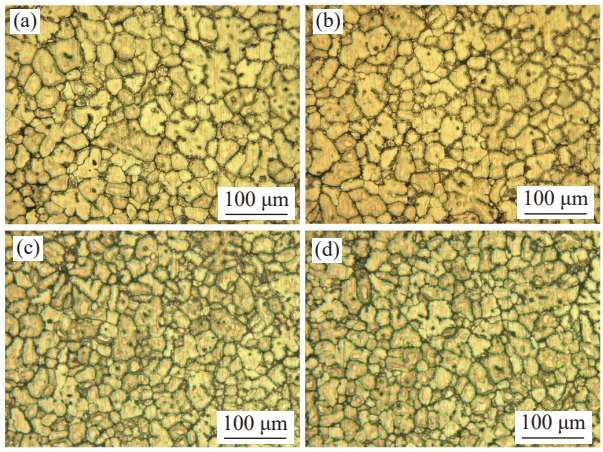

Fig. 2. Optical microscopy images of Al7075–CNTs ANCs: (a) A_0; (b) $A_{0.5}$; (c) A_1; (d) $A_{1.5}$.

3.2.3. TEM analysis

Fig. 5(a–d) shows the TEM characterization of solutionized and aged Al7075 with 0 and 1wt% CNTs, and Fig. 5(e) shows the CNTs interlayer spacing. Fig. 5(a–b) depicts the dislocation density in the T_0 nanocomposite, and the related enlarged view. Owing to the thermal mismatch of the ANCs, the existence of second-phase particles, and the separation of solute elements, dislocation density is formed [31]. Because of the RUMS process, the CNTs are randomly dispersed in the matrix because of the presence of homogeneously dispersed CNTs of T_1 ANCs, as shown in Fig. 5(c–d). The high dislocation density in the ANCs increases its strength with

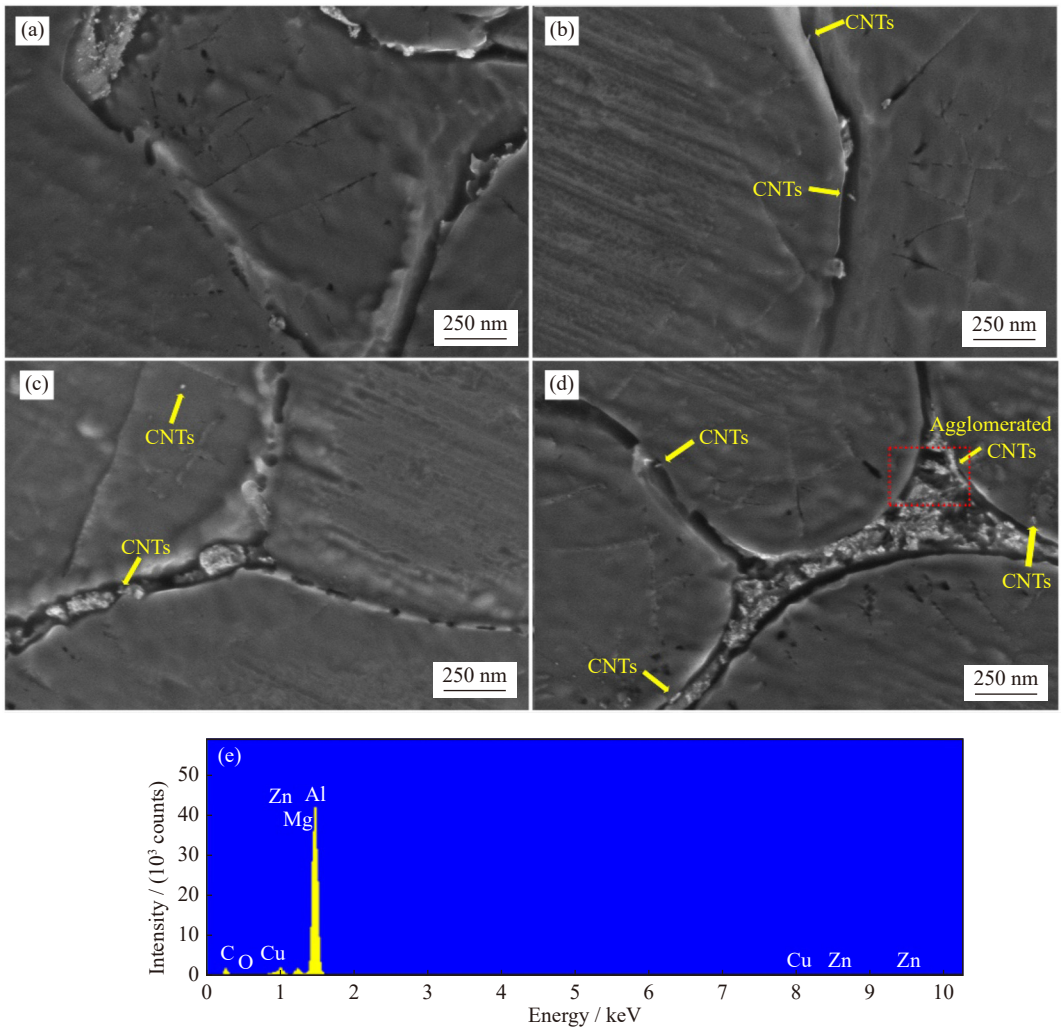

Fig. 3. SEM images of Al7075–CNTs ANCs: (a) A_0, (b) $A_{0.5}$, (c) A_1, and (d) $A_{1.5}$; (e) EDS at the grain boundary in (d).

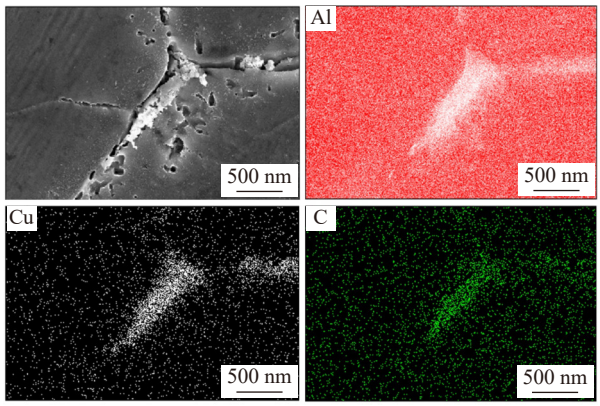

Fig. 4. SEM image and elemental mapping of the A_1 ANCs sample.

1wt% CNTs. The presence of dislocations in the Al matrix with uniformly dispersed CNTs prevents slip movement during deformations as they associate with the precipitates. Dislocation resistance offered by interaction with second-phase particles and reinforcements requires high stress for deformation. Thus, the ANCs with 1wt% CNTs improve mechanical properties. Inside the grain are well-spaced CNTs, with no indication of adjacent grain boundaries and agglomerations. No interfacial oxide deposits, reaction products, or other defects are observed at the Al matrix/CNTs reinforcement interface.

The ANCs also undergo a solutionizing and aging process, according to ASTM T6 specifications (490°C/1 h for heat treating the solution and 120°C/24 h for annealing). There are more η phases in this state of nanocomposites, as well as fewer Guinier–Preston (GP) zones (GP1 and GP2) and metastable ($MgZn_2$) phases. At the interface plane, the two lattices are continuous, and the arrangement of alloying atoms in the GP zone and matrix phase coincide. GP zones cause the surrounding lattice to experience considerable strain, which prevents dislocation slip. Although the lattice strain imposes resistance against slip and hardens the metal, dislocations can nevertheless shear through GP zones [32].

3.2.4. X-ray diffraction (XRD)

Fig. S4 shows the XRD patterns for the ANCs with various content of CNTs under solutionized and aged conditions. All the curves have similar positions for the Al matrix phase peaks. The precipitate phases are represented by intermediate, tiny peaks in the aluminum matrix phase peaks. The $MgZn_2$ (η) phases, which are presented in the ANCs, are the most dominant precipitates [33]. $Mg(Al, Cu, Zn)_2$ phases can occur in the ANCs because they have a related crystallographic lattice parameter of $MgZn_2$ [34]. After the solutionizing and aging (T6 heat-treated condition) of the ANCs, the Al_2CuMg phase occurred, while the $Mg(Al, Cu, Zn)_2$ phase was eliminated. The Al_7Cu_2Fe phase also exists in all ANCs samples, and the peak overlaps with the ANCs matrix peak. the intensity of CNTs peaks are very weak due to the low content of CNTs when correlated with aluminum matrix peaks and other second-phase particle peaks. Hence, the XRD peaks of CNTs are not apparent in the XRD graph.

3.3. Mechanical properties

3.3.1. Microhardness

The Vickers hardness test of both sets of samples is performed as per the ASTM standard. The increase in the hardness value, as shown in Fig. 6, is related to the presence of CNTs, which have a smaller separation and prevent disloca-

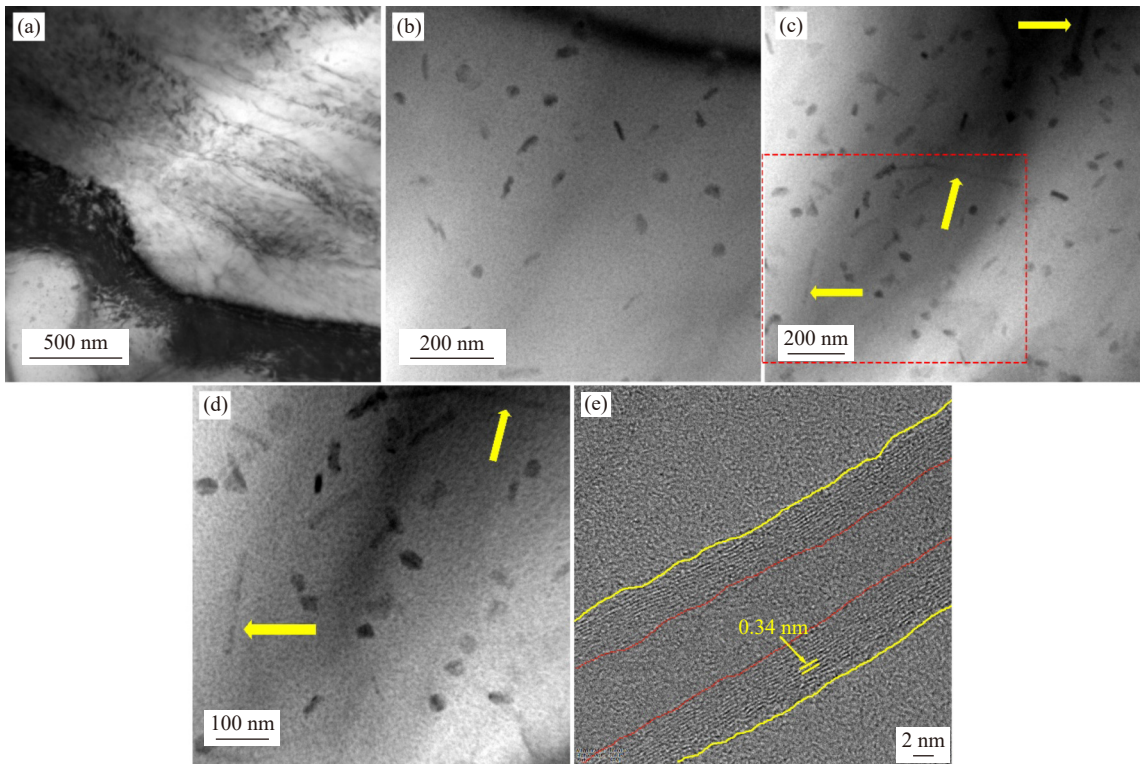

Fig. 5. TEM characterization of ANCs with different weight percentage of CNTs: (a–b) T_0; (c–d) T_1; (e) interlayer spacing of CNTs.

tion movement [35]. The increase in hardness value indicates that CNTs are involved in the formation of crystal structure in the ANCs and that the nanofillers inhibit grain growth via a pinning action, resulting in increased grain size reduction. The Hall–Petch equation states that the average grain diameter is inversely related to the strength of the ANCs.

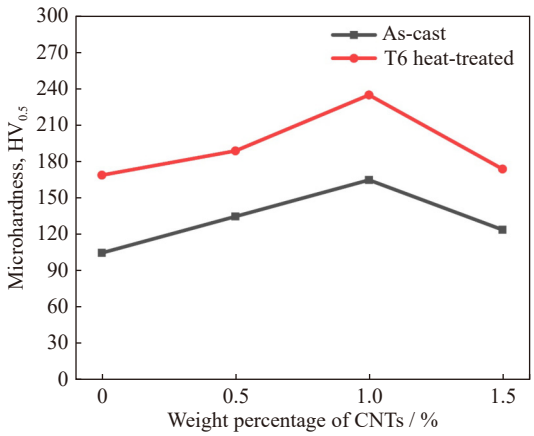

Fig. 6. Vickers microhardness of the as-cast and T6 heat-treated ANCs samples.

The interfacial bond between Al7075 and the CNTs, the hindering influence of dislocation motions, and improved grain refinement are the main reasons for the improvement in the microhardness of the nanocomposites. Because of the homogeneous distribution of CNTs, the magnitude of hardness increases until 1wt% CNTs, while further increase in content of CNTs does not improve hardness, as shown in Fig. 6. This is attributed to the clustering of CNTs reinforcements. Barati F *et al*. [36] found that the hardness of nanocomposites reinforced with 2wt% CNTs is considerably reduced, which is most likely due to the cluster formation of nanotubes during agglomeration.

3.3.2. Tensile strength

Three of the four as-cast and heat-treated samples of the ANCs are subjected to the tensile test, and the ultimate tensile strength (UTS) and percentage elongation values are calculated using the average of the three results. A graphical illustration of percentage elongation and UTS for the ANCs under various conditions is shown in Fig. 7.

A rising trend is evident in the ultimate strength and elongation of the ANCs. As the content increased, the mechanical properties of the material deteriorated. During the RUMS process, the acoustic streaming effect disperses the cavitation voids in the low-pressure zone, resulting in a homogenous dispersion in the Al matrix, and thus agglomerations are avoided. Further inclusion of CNTs in the Al matrix forms CNTs clustering in the matrix, which reduces strength and percentage elongation (Fig. 7).

The strength of the ANCs is influenced by the wide surface interfacial areas of CNTs as well as its ability to shift loads [37–38]. The presence of solid-phase CNTs in the Al7075 matrix, which confines the slip movement of the ANCs along with crack generation while allowing atoms to

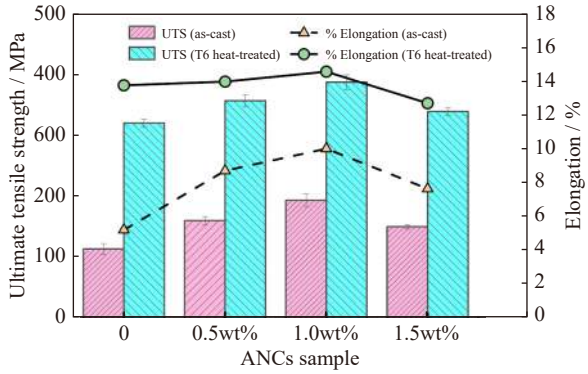

Fig. 7. UTS and elongation for the ANCs under various circumstances.

slide over each other, results in higher tensile values. With the addition of CNTs, the Orowan strengthening effect caused by slip formation inside the ANCs inhibits crack propagation [39]. Therefore, it is linked to the consistent scattering of CNTs in aluminum, which enhances mechanical strength. Furthermore, RUMS and the inclusion of CNTs particles reduce grain size and increase grain boundaries (Hall–Petch strengthening). The mechanical strength of the ANCs is greatly influenced by the shape and grain size of the materials. As the CNTs content increases, the grain size increases, resulting in a decrease in the ultimate tensile strength and elongation of the ANCs.

Thermal stresses are induced in the nanocomposites because of the preheated state of the CNTs added during the casting process. Preheated nanoparticles are used to improve the interfacial adhesion between the matrix and the second-phase particles. The thermal disparity between Al7075 and CNTs explains the higher UTS values [40]. The interaction between CNTs and the Al matrix has been attributed to grain detachment as surface energy increases. Under tensile loading conditions, adjacent crystals and the interfacial friction of particles increase [41–42].

Fig. 8 shows tensile fractography images of solutionized and aged ANCs (0 and 1wt% CNTs). As can be seen, the fractured tensile surface with globular dendrites and tear ridges is observed in pure ANCs, and it indicate brittle fail-

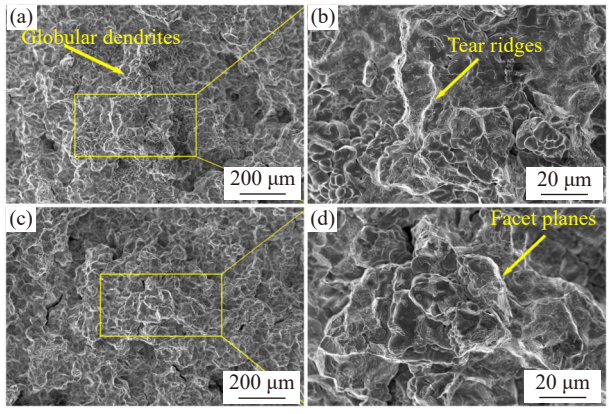

Fig. 8. SEM images for tensile fractured samples of Al7075–CNTs ANCs: (a) T_0; (b) an enlarged view of T_0; (c) T_1; (d) an enlarged view of T_1.

ure (Fig. 8(a–b)). Fig. 8(c–d) shows an enhanced fractured tensile image of the ANCs with 1wt% CNTs, displaying facet planes and a few microvoids developed by the grain separation effect [43]. Thus, a semi-brittle fracture mechanism is demonstrated for the ANCs with 1wt% CNTs, which accounts for the enhanced mechanical properties. Thus, this fracture study shows failure modes that are partially brittle and ductile.

3.3.3. Impact test

Impact loading causes internal damage to the structural components of the robot, resulting in performance failures. Materials with a high capacity to absorb applied forces are required for structural applications. All of the composites show an increase in impact toughness. This increase could be assigned to the combined crack dispersion restriction of precipitates and distributed particles. Because the impact toughness of the fabricated composites is a crucial feature for component designers, it is investigated in this work and reported in Fig. 9. A comparison of the results shows that the presence of CNTs allows absorption of maximum energy on the Al matrix. This result is attributed to the ability of these particles to stop crack growth. The T_1 ANCs has higher impact toughness than other ANCs because of grain refinement and particle dispersion in the Al matrix [44].

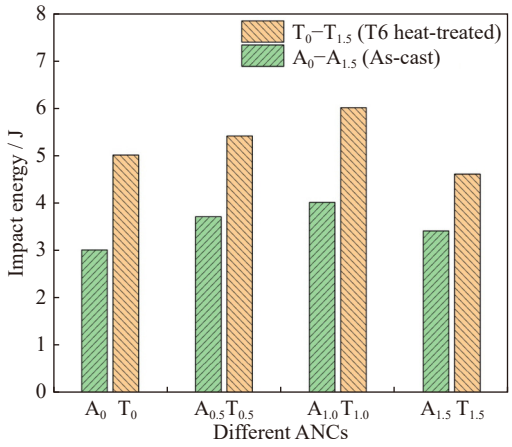

Fig. 9. Impact test of nanocomposites under as-cast and heat-treated conditions.

Fig. 10(a–b) shows a fractured impact surface with intergranular fracture and ductile failure for the ANCs without CNTs, and Fig. 10(c–d) shows a fractured impact surface with transgranular fracture, cleavage facets, and microvoids for the ANCs with 1wt% CNTs, indicating partial ductile and brittle failure.

The hardness, UTS, and impact values of T1 increased by 42.24%, 100.23%, and 50%, respectively, in comparison to the A1 ANCs, with both ANCs having 1wt% CNTs. In comparison with the base metal (A0), the hardness, UTS, and impact values of T0 increased by 60.95%, 181.041%, and 66.67%, respectively.

3.4. Corrosion test

3.4.1. Salt spray corrosion test

According to research observations, the cathodic and anodic processes responsible for aluminum alloy corrosion in an aerated CH_3COOH solution are dissolved oxygen reduction and aluminum alloy oxidation. According to the point defect model, acetate ions displace oxygen in the oxide film and compete with cation vacancies to produce metal acetate, degrading the oxide film and triggering the pitting process, as shown in Fig. 11. Galvanic coupling between the precipitates of the second phase and the matrix of the ANCs results in anodic dissolution. Acetate ions can expedite the corrosion of the top layer of the ANCs by rupturing the oxide film [45].

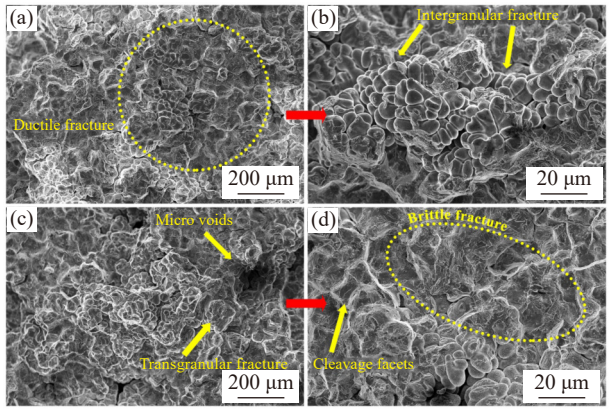

Fig. 10. SEM images for impact fractography of Al7075–CNTs ANCs: (a) T_0; (b) enlarged view of T_0; (c) T_1; (d) enlarged view of T_1.

According to the XRD of the ANC, the intermetallics of the A17075 alloy are primarily composed of Al_7Cu_2Fe, $(Al, Cu)_6(Fe, Cu)$, and Mg_2Si. Because Mg_2Si has a higher corrosion potential than the other Al phases, this phase dissolves, first causing pitting corrosion. Local corrosion uses Al_7Cu_2Fe and $(Al, Cu)_6(Fe, Cu)$ as cathodes to accelerate the corrosion of the surrounding matrix because they have higher corrosion potentials than the matrix [46].

Although $MgZn_2$ is the primary precipitated strengthening phase, it dissolves faster than the matrix as an anode because of its higher corrosion potential than the other Al phases. Because of the interaction between the expansion of corrosion products and the external corrosion media, corrosion cracks began to form on the Al alloy surface. As the cracks progress, the Al plate corrodes, and the layered surface spalling phenomenon emerges, as shown in Fig. 12. The inclusion of CNTs may cause a slight decrease in permeability, which decreases the infiltration of aggressive chemicals and delays the onset of corrosion. This delay eventually causes corrosion to slow down, which will prolong the life of the robot.

3.4.2. Immersion test

The corrosion resistance of solutionized and aged (T6) CNTs ANCs specimens of various content of CNTs is higher than that of the other as-cast CNTs ANCs specimens, as shown in Fig. 13(a–b). The graph shows that the T_1 ANCs specimen lose less weight per year compared to the other specimens.

After 5 days of immersion, all specimens show certain

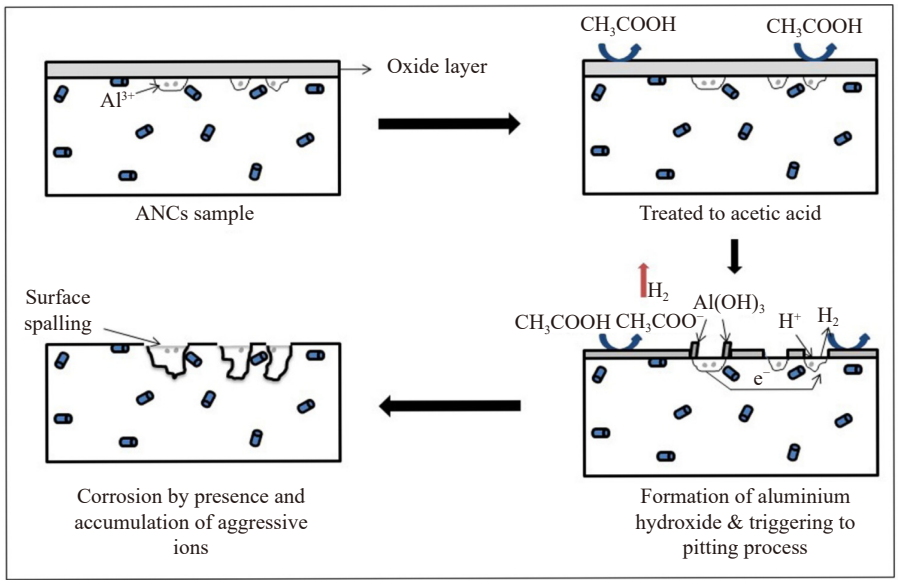

Fig. 11. Corrosion mechanism of the ANCs.

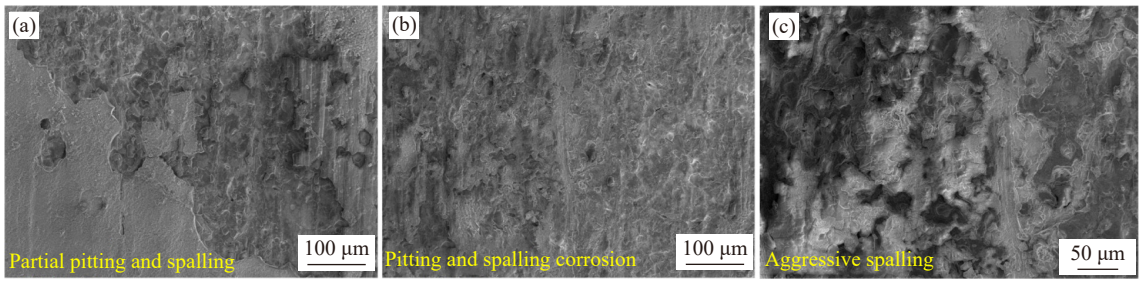

Fig. 12. SEM images for salt fog corrosion of the T_1 ANCs in the acetic acid solution under different time: (a) 24 h; (b) 72 h; (c) 120 h.

evidence of pitting corrosion, and the pit density and size increase over time. Fig. 13(c–f) shows the 3D surface graph of the immersion test in various concentrations of the acetic acid solution for heat treated samples. As can be seen, the T_1 ANCs sample has less weight loss per year compared to others. However, the sorption capacity of the acetate ions in the as-cast ANCs is greater than that of the ANCs heattreated samples.

Additionally, the creation of hydrogen through a cathodic reaction near active pit sites causes the development of bubbles at the pit mouth [47]. Fig. 14 shows the corroded surface of the solutionized and aged ANCs. Obviously, fewer pits are seen in the $T_{0.5}$ ANCs sample. The T_0 ANCs sample has deeper and broader holes than the T_1 ANCs sample. The formation of larger and deeper pits is associated with the presence of large grains and precipitates on the T_0 surface, as shown in Fig. 14(d).

The order of the pit average size is observed as $T_1 < T_{0.5} < T_{1.5} < T_0$, indicating that the T_1 sample has better corrosion resistance than other samples. Al–Zn–Mg–(Cu) alloys, such as Al7075, are well known to experience severe attacks along grain boundaries in acetic acid solutions. Intergranular corrosion of these alloys occurs because of certain precipitates at or near the grain boundary area. A substantial corrosion attack occurs at the grain boundary or the precipitate-free zone along the grains. This result is due to grain boundary precipitations acting as either anodes or cathodes to the aluminum matrix.

3.4.3. Potentiodynamic polarization test

Fig. 15 shows the potentiodynamic polarization (PDP) curves developed from the electrochemical testing of heat-treated ANCs specimens. Al resistance is widely known to be correlated with a fine and concise coating of naturally generated oxide on the surface of a metal; however, this oxide layer is only stable in the pH range of 4–8. Lower or higher pH values destroy the protective barrier, resulting in considerable metal dissolution [48].

The corrosion in the Al matrix is probably due to the impurities in the Al alloy, particularly Mg (2.325wt%) and Fe (0.089wt%). These precipitate impurities merely weaken the resistance to corrosion of the Al alloy by enhancing the cathodic volume fraction, even when their quantity is low. Additionally, alloying components are typically found in intermetallic compounds and aqueous solutions of aluminum, both of which have a significant impact on how ANCs behave when subjected to corrosion. A smaller crystallite size, the presence of CNTs, decreased intermetallic phases, and the textural effect are the major aspects that influence the corrosion resistance of the composites. The CNTs in the matrix behave as a cathode, causing galvanic action. When all of these parameters are combined, the corrosion behavior of the composite is marginally better than that of Al7075 base metal.

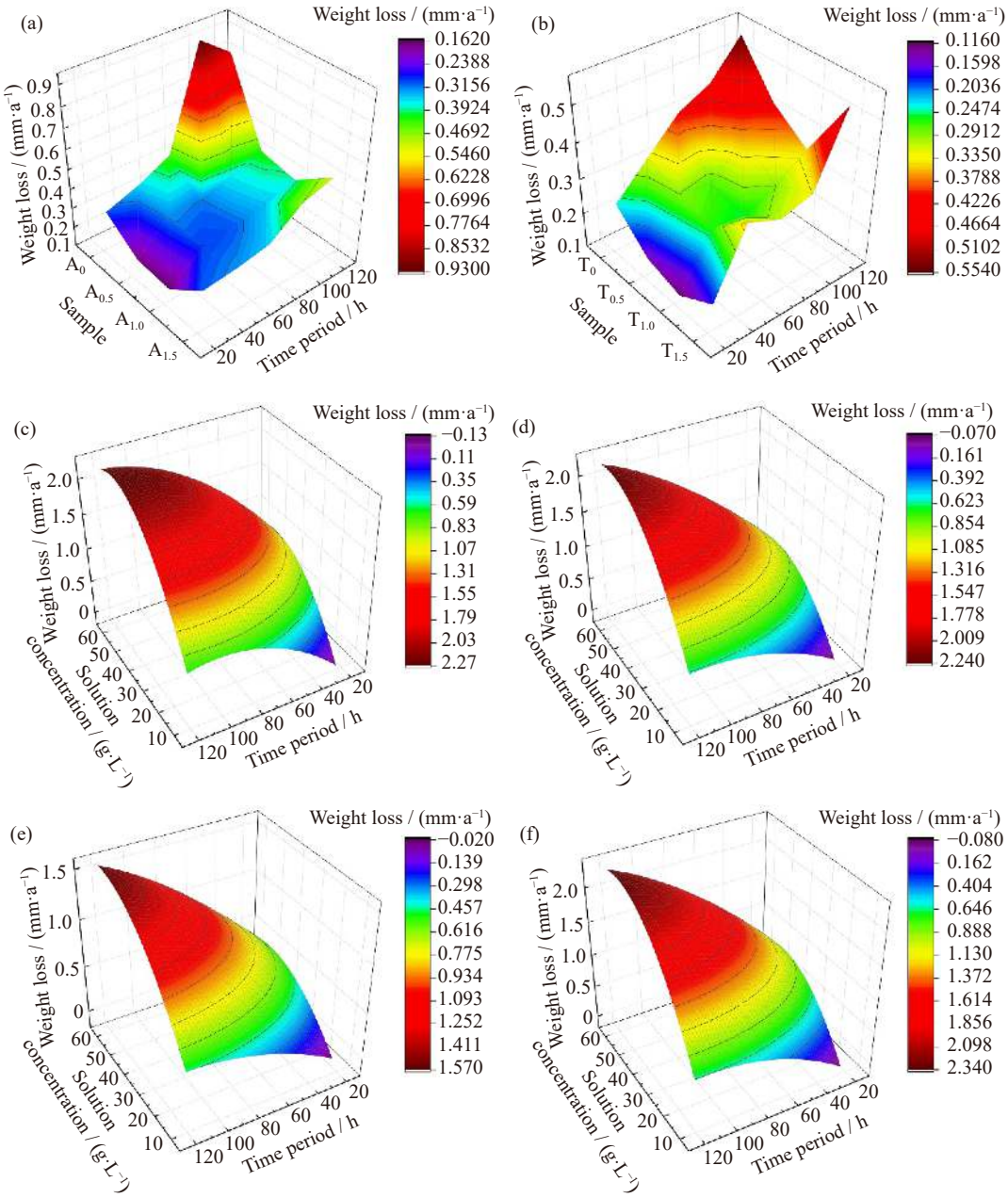

Fig. 13. 3D surface graphs of as-cast salt fog (a), heat treated (b), (c–f) immersion corrosion tests of the (c) T_0, (d) $T_{0.5}$, (e) T_1, and (f) $T_{1.5}$ ANCs samples.

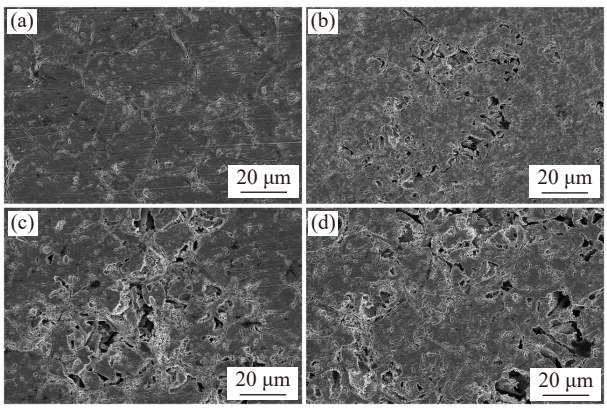

Fig. 14. SEM images for immersion corrosion of 40wt% acetic acid solution for 72 h: (a) T_1; (b) $T_{0.5}$; (c) $T_{1.5}$; (d) T_0 ANCs samples.

In an electrolyte, the corrosion potential (E_{corr}) is generally influenced by the alloy composition, solute content in the solid solution, volume fraction, size, and the presence of second-phase elements, and other factors [49]. By using the Tafel extrapolation approach, the corrosion current density (i_{corr}) of the Al7075 alloy and the composites are calculated from the polarization curves (Fig. 15). Table 4 lists the Tafel constants for the alloys and composites as well as electrochemical information such as corrosion potential (E_{corr}), polarization resistance (R_p), and corrosion current density (i_{corr}).

In terms of corrosion potential (E_{corr}), 1wt% ANCs performed slightly better than the other three ANCs. The corrosion current density (i_{corr}) of T_1 is slightly lower than that of other ANCs samples, indicating improved corrosion behavior. Therefore, this study firmly establishes that the RUMS

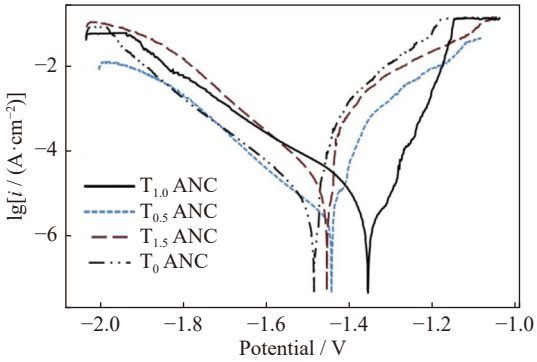

Fig. 15. Potentiodynamic polarization curves of T_0, $T_{0.5}$, T_1, and $T_{1.5}$ ANCs samples.

Table 4. Electrochemical data of Al7075–CNTs (0, 0.5wt%, 1wt%, and 1.5wt%) composites in acetic acid solution

Composite	E_{corr} / V	i_{corr} / (10^{-6} A·cm^{-2})	R_p / Ω	Corrosion rate / (mm·a^{-1})
T_0	–1.4897	207.5	241	4.9030
$T_{0.5}$	–1.4326	7.835	6382	0.1851
T_1	–1.3681	6.893	7253	0.1629
$T_{1.5}$	–1.4495	14.51	3446	0.3429

method may be used to generate a surface ANCs with enhanced mechanical properties without compromising corrosion performance.

4. Conclusions

The RUMS method is used to fabricate Al7075–CNTs nanocomposites (0, 0.5wt%, 1wt%, and 1.5wt% CNTs) and an equal number of heat treated samples. Based on the studies on ANCs samples, the following conclusions are drawn: (1) The AGS decreased with increasing reinforcement in the Al matrix. T_1 has the lowest AGS. (2) The presence and dispersion of CNTs are examined using SEM–EDS analysis, and XRD shows the different phases present in the ANCs. The dislocation density and presence of CNTs are determined using TEM. The SEM fractography shows a partial brittle and ductile fracture mechanism, tear ridges, and intergranular as well as transgranular fractures. (3) By adding 1wt% CNTs, the hardness, UTS, and impact values of T_1 increased by 42.24%, 100.23%, and 50%, respectively, compared to the A_1 ANCs. T_0 increased by 60.95%, 181.041%, and 66.67%, respectively, compared to the base metal. (4) Pitting, surface spalling, and intergranular corrosion are the primary causes of corrosion, as determined using salt spray and immersion corrosion tests. T_1 has better corrosion resistance than other ANCs samples. (5) The PDP curves exhibit active behavior throughout the entire range of the applied potential for each composition. T_1, again, is found to have better corrosion resistance, which is attributed to the fine-grain structure and the presence of CNTs.

Hence, T_1 ANCs stand out as a better candidate for building a robot for in-pipe applications for better performance in corrosive environments without compromising the mechanical performance characteristics of the robot. The results obtained could be validated for optimized corrosion and mechanical performance once the prototype of the robot is developed.

Acknowledgements

This work was supported by the Government of India's Department of Science and Technology (DST) and Science and Engineering Research (SERB) Board (Nos. ECR/2016/001193 and CRG/2018/001006).

Conflict of Interest

The authors declared no potential conflicts of interest with respect to the research, authorship, and/or publication of this article.

Supplementary Information

The online version contains supplementary material available at https://doi.org/10.1007/s12613-022-2592-3.

References

[1] R.K. Bhushan and S. Kumar, Influence of SiC particles distribution and their weight percentage on 7075 Al alloy, *J. Mater. Eng. Perform.*, 20(2011), No. 2, p. 317.

[2] A. Kalkanlı and S. Yılmaz, Synthesis and characterization of aluminum alloy 7075 reinforced with silicon carbide particulates, *Mater. Des.*, 29(2008), No. 4, p. 775.

[3] S.M. Choi and H. Awaji, Nanocomposites–A new material design concept, *Sci. Technol. Adv. Mater.*, 6(2005), No. 1, p. 2.

[4] S. Gopalakannan and T. Senthilvelan, Synthesis and characterisation of Al7075 reinforced with SiC and B_4C nano particles fabricated by ultrasonic cavitation method, *J. Sci. Ind. Res.*, 74(2015), No. 5, p. 281.

[5] M. Imran and A.R.A. Khan, Characterization of Al-7075 metal matrix composites: A review, *J. Mater. Res. Technol.*, 8(2019), No. 3, p. 3347.

[6] A. Baradeswaran and A.E. Perumal, Study on mechanical and wear properties of Al7075/Al_2O_3/graphite hybrid composites, *Composites Part B*, 56(2014), p. 464.

[7] A. Baradeswaran and A.E. Perumal, Wear and mechanical characteristics of Al7075/graphite composites, *Composites Part B*, 56(2014), p. 472.

[8] A.I. Khdair and A. Fathy, Enhanced strength and ductility of Al–SiC nanocomposites synthesized by accumulative roll bonding, *J. Mater. Res. Technol.*, 9(2020), No. 1, p. 478.

[9] G.B.V. Kumar, C.S.P. Rao, N. Selvaraj, and M.S. Bhagyashekar, Studies on Al6061–SiC and Al7075–Al_2O_3 metal matrix composites, *J. Miner. Mater. Charact. Eng.*, 9(2010), No. 1, p. 43.

[10] M.H. Jokhio, M.I. Panhwer, and M.A. Unar, Manufacturing of aluminum composite material using stir casting process, *Mehran Uni. Res. J. Eng. Technol.*, 30(2016), No. 1, p. 53.

[11] A. Pardo, M.C. Merino, S. Merino, F. Viejo, M. Carboneras, and R. Arrabal, Influence of reinforcement proportion and matrix composition on pitting corrosion behaviour of cast aluminium matrix composites (A3xx.x/SiCp), *Corros. Sci.*, 47(2005), No. 7, p. 1750.

[12] G.M. Pinto, N. Nayak, and A. Nityananda Shetty, Corrosion behaviour of 6061 Al–15vol. Pct. SiC composite and its base alloy in a mixture of 1 : 1 hydrochloric and sulphuric acid medium, *Int. J. Electrochem. Sci.*, 4(2009), No. 10, p. 1452.
[13] F. Toptan, A.C. Alves, I. Kerti, E. Ariza, and L.A. Rocha, Corrosion and tribocorrosion behaviour of Al–Si–Cu–Mg alloy and its composites reinforced with B_4C particles in 0.05 M NaCl solution, *Wear*, 306(2013), No. 1-2, p. 27.
[14] S. Candan, An investigation on corrosion behaviour of pressure infiltrated Al–Mg alloy/SiC_p composites, *Corros. Sci.*, 51 (2009), No. 6, p. 1392.
[15] J.F Li, Z.W. Peng, C.X. Li, Z.Q. Jia, W.J. Chen, and Z.Q. Zheng, Mechanical properties, corrosion behaviors and microstructures of 7075 aluminium alloy with various aging treatments, *Trans. Nonferrous Met. Soc. China*, 18(2008), No. 4, p. 755.
[16] P. Liu, S.E. Yang, Y.S. Chen, *et al*., Carbon nanotube-based heterostructures for high-performance photodetectors: Recent progress and future prospects, *Ceram. Int.*, 46(2020), No. 12, p. 19655.
[17] Y. Zhang, Q. Wang, G. Chen, and C.S. Ramachandran, Mechanical, tribological and corrosion physiognomies of CNT–Al metal matrix composite (MMC) coatings deposited by cold gas dynamic spray (CGDS) process, *Surf. Coat. Technol.*, 403(2020), art. No. 126380.
[18] B. Chen, K. Kondoh, J. S. Li, and M. Qian, Extraordinary reinforcing effect of carbon nanotubes in aluminium matrix composites assisted by *in situ* alumina nanoparticles, *Composites Part B*, 183(2020), art. No. 107691.
[19] T. Laha, A. Agarwal, T. McKechnie, and S. Seal, Synthesis and characterization of plasma spray formed carbon nanotube reinforced aluminum composite, *Mater. Sci. Eng. A*, 381(2004), No. 1-2, p. 249.
[20] A. Rutkowska, T.M. Bawazeer, J.V. Macpherson, and P.R. Unwin, Visualisation of electrochemical processes at optically transparent carbon nanotube ultramicroelectrodes (OT–CNT–UMEs), *Phys. Chem. Chem. Phys.*, 13(2011), No. 12, p. 5223.
[21] C.F. Deng, X.X. Zhang, D.Z. Wang, Q. Lin, and A.B. Li, Preparation and characterization of carbon nanotubes/aluminum matrix composites, *Mater. Lett.*, 61(2007), No. 8-9, p. 1725.
[22] C.F. Deng, D.Z. Wang, X.X. Zhang, and A.B. Li, Processing and properties of carbon nanotubes reinforced aluminum composites, *Mater. Sci. Eng. A*, 444(2007), No. 1-2, p. 138.
[23] S.I. Ghazanlou and B. Eghbali, Fabrication and characterization of GNPs and CNTs reinforced Al7075 matrix composites through the stir casting process, *Int. J. Miner. Metall. Mater.*, 28(2021), No. 7, p. 1204.
[24] I. Sridhar and K.R. Narayanan, Processing and characterization of MWCNT reinforced aluminum matrix composites, *J. Mater. Sci.*, 44(2009), No. 7, p. 1750.
[25] C. Kannan and R. Ramanujam, Comparative study on the mechanical and microstructural characterisation of AA 7075 nano and hybrid nanocomposites produced by stir and squeeze casting, *J. Adv. Res.*, 8(2017), No. 4, p. 309.
[26] T. Laha, Y. Chen, D. Lahiri, and A. Agarwal, Tensile properties of carbon nanotube reinforced aluminum nanocomposite fabricated by plasma spray forming, *Compos. A Appl. Sci. Manuf.*, 40(2009), No. 5, p. 589.
[27] V.V. Shanbhag, N.N. Yalamoori, S. Karthikeyan, R. Ramanujam, and K. Venkatesan, Fabrication, surface morphology and corrosion investigation of Al7075–Al_2O_3 matrix composite in sea water and industrial environment, *Procedia Eng.*, 97(2014), p. 607.
[28] S.C. Amith and P. Lakshmanan, Effects of simultaneous rotational ultrasonication and vortex-induced casting technique on particle distribution and grain refinement in AA7075/h-BN nanocomposites, *Proc. Inst. Mech. Eng. Part L J. Mater. Des. Appl.*, 236(2022), No. 8, p. 1648.
[29] B. Abbasipour, B. Niroumand, S.M. Monir Vaghefi, and M. Abedi, Tribological behavior of A356–CNT nanocomposites fabricated by various casting techniques, *Trans. Nonferrous Met. Soc. China*, 29(2019), No. 10, p. 1993.
[30] H. Liao, Y. Sun, and G. Sun, Correlation between mechanical properties and amount of dendritic α-Al phase in as-cast near-eutectic Al-11.6% Si alloys modified with strontium, *Mater. Sci. Eng. A*, 335(2002), No. 1-2, p. 62.
[31] G. Anne, M.R. Ramesh, S.B. Arya, and S. Sahu, Microstructure evolution and mechanical and corrosion behavior of accumulative roll bonded Mg–2%Zn/Al-7075 multilayered composite, *J. Mater. Eng. Perform.*, 26(2017), No. 4, p. 1726.
[32] A.P. Mouritz, *Introduction to Aerospace Materials*, Amsterdam: Elsevier, 2012.
[33] K. Mohan, J.A. Suresh, P. Ramu, and R. Jayaganthan, Microstructure and mechanical behavior of Al7075–T6 subjected to shallow cryogenic treatment, *J. Mater. Eng. Perform.*, 25(2016), No. 6, p. 2185.
[34] N. Yazdian, F. Karimzadeh, and M. Tavoosi, Microstructural evolution of nanostructure 7075 aluminum alloy during isothermal annealing, *J. Alloys Compd.*, 493(2010), No. 1-2, p. 137.
[35] H. Hashim, M.S. Salleh, M.Z. Omar, and A.B. Sulong, Optimisation of mechanical stir casting parameters for fabrication of carbon nanotubes-aluminium alloy composite through Taguchi method, *J. Mater. Res. Technol.*, 8(2019), No. 2, p. 2223.
[36] F. Barati and M. Esfandiari, The effect of multi-walled carbon nanotubes, as the reinforcement phase, on the hardness and bending strength of aluminum alloy 7075, *J. Stress Anal.*, 6(2021), No. 1, p. 61.
[37] H. Puga, V.H. Carneiro, J. Barbosa, and D. Soares, Effect of grain and secondary phase morphologies in the mechanical and damping behavior of Al7075 alloys, *Met. Mater. Int.*, 22(2016), No. 5, p. 863.
[38] A. Kumar, K. Pal, and S. Mula, Simultaneous improvement of mechanical strength, ductility and corrosion resistance of stir cast Al7075–2% SiC micro- and nanocomposites by friction stir processing, *J. Manuf. Process.*, 30(2017), p. 1.
[39] R.A. Manikandan and T.V. Arjunan, Studies on micro structural characteristics, mechanical and tribological behaviours of boron carbide and cow dung ash reinforced aluminium (Al 7075) hybrid metal matrix composite, *Composites Part B*, 183(2020), art. No. 107668.
[40] P. Samal, P.R. Vundavilli, A. Meher, and M.M. Mahapatra, Reinforcing effect of multi-walled carbon nanotubes on microstructure and mechanical behavior of AA5052 composites assisted by *in situ* TiC particles, *Ceram. Int.*, 48(2022), No. 6, p. 8245.
[41] X.F. Wang, M.X. Guo, C.Q. Ma, J.B. Chen, J.S. Zhang, and L.Z. Zhuang, Effect of particle size distribution on the microstructure, texture, and mechanical properties of Al–Mg–Si–Cu alloy, *Int. J. Miner. Metall. Mater.*, 25(2018), No. 8, p. 957.
[42] S. Suresh, G.H Gowd, and M.L. Deva Kumar, Mechanical properties of AA 7075/Al_2O_3/SiC nano-metal matrix composites by stir-casting method, *J. Inst. Eng. India Ser. D*, 100(2019), No. 1, p. 43.

[43] A. Pineau, A.A. Benzerga, and T. Pardoen, Failure of metals I: Brittle and ductile fracture, *Acta Mater.*, 107(2016), p. 424.

[44] H.A Deore, J. Mishra, A.G. Rao, H. Mehtani, and V.D. Hiwarkar, Effect of filler material and post process ageing treatment on microstructure, mechanical properties and wear behaviour of friction stir processed AA 7075 surface composites, *Surf. Coat. Technol.*, 374(2019), p. 52.

[45] B. Zhou, B. Liu, S.G. Zhang, R. Lin, Y. Jiang, and X.Y. Lan, Microstructure evolution of recycled 7075 aluminum alloy and its mechanical and corrosion properties, *J. Alloys Compd.*, 879(2021), art. No. 160407.

[46] F. Andreatta, H. Terryn, and J.H.W. De Wit, Effect of solution heat treatment on galvanic coupling between intermetallics and matrix in AA7075–T6, *Corros. Sci.*, 45(2003), No. 8, p. 1733.

[47] M. Navaser and M. Atapour, Effect of friction stir processing on pitting corrosion and intergranular attack of 7075 aluminum alloy, *J. Mater. Sci. Technol.*, 33(2017), No. 2, p. 155.

[48] J. Halambek, M.C. Bubalo, I.R. Redovniković, and K. Berković, Corrosion behaviour of aluminium and AA5754 alloy in 1% acetic acid solution in presence of laurel oil, *Int. J. Electrochem. Sci*, 9(2014), No. 10, p. 5496.

[49] K.S. Ghosh, S. Mukhopadhyay, B. Konar, and B. Mishra, Study of aging and electrochemical behaviour of Al–Li–Cu–Mg alloys, *Mater. Corros.*, 64(2013), No. 10, p. 890.